Nonlinear ballooning instability in the near-Earth magnetotail: Growth, structure, and possible role in substorms

P. Zhu,[1] C. R. Sovinec,[1] C. C. Hegna,[1] A. Bhattacharjee,[2] and K. Germaschewski[2]

Received 28 July 2006; revised 6 February 2007; accepted 19 February 2007; published 14 June 2007.

[1] To examine the scenario that the onset of a substorm can be triggered by ballooning instabilities in the near-Earth magnetotail, we have performed three-dimensional direct magnetohydrodynamic simulations of the nonlinear evolution of the ideal ballooning instability in two types of analytic Grad-Shafranov equilibria of the magnetotail. The nonlinear growth and spatial structure (in both real and spectral spaces) of the instability are obtained for both classes of equilibria, and its observable consequences are explored. In particular, the linearly unstable ballooning mode is demonstrated to grow exponentially in the early nonlinear phase, and it starts to slow down or saturate in the intermediate nonlinear phase. The intermediate nonlinear phase is characterized by the formation of fine-scale patterns determined by the dominant k_y mode and spatially discontinuous structures that tend to accumulate at the stagnation point of the sheared flow profile spontaneously generated by the instability. It is proposed that, unlike the predictions of a theory of explosive nonlinear growth, the nonlinear ballooning instability, by itself, cannot produce a current disruption. However, the possibility remains open that the ballooning instability, when coupled to current-driven instabilities and nonideal mechanisms such as reconnection and turbulent transport, may produce current sheet disruption in the near-Earth magnetotail.

Citation: Zhu, P., C. R. Sovinec, C. C. Hegna, A. Bhattacharjee, and K. Germaschewski (2007), Nonlinear ballooning instability in the near-Earth magnetotail: Growth, structure, and possible role in substorms, *J. Geophys. Res.*, *112*, A06222, doi:10.1029/2006JA011991.

1. Introduction

[2] The purpose of this work is to examine the possible role of the nonlinear ballooning instability in the near-Earth magnetotail during the substorm onset process by means of direct MHD simulations. We attempt to address the following questions: Is the nonlinear growth of the ballooning instability faster than the linear phase? Can the nonlinear growth directly account for the timescale of the current sheet disruption? How does the nonlinear ballooning instability reconfigure the current sheet prior to the onset of disruption? What are the unique signatures and spatial patterns of the nonlinear ballooning instability that can be identified in observations?

[3] The idea that substorm onsets may be triggered by the ballooning instability of the near-Earth magnetotail has been mainly motivated by several pieces of suggestive observational evidence. Early ground ionospheric observations [*Atkinson*, 1967; *Kisabeth and Rostoker*, 1971] and recent conjunct satellite and ground observations [*Lopez and Lui*, 1990; *Lopez et al.*, 1990; *Samson et al.*, 1992a, 1992b; *Sergeev et al.*, 1993; *Frank and Sigwarth*, 2000; *Friedrich et al.*, 2001] of substorm auroral dynamics provide evidence of near-Earth tail activities that are directly associated with the onset of a substorm [for a recent review, see *Lui*, 2003]. In particular, *Roux et al.* [1991] suggested that the westward traveling surge observed by the all-sky camera during a substorm was the image of plasma sheet instability in the magnetotail. Within the magnetotail, in situ satellite observations indicate that the near-Earth current sheet breakup prior to substorm onset can take place in the absence of Earthward fast flow that is often attributed to middle-magnetotail reconnection, whereas the Earthward fast flow from midtail reconnection does not necessarily trigger a substorm onset [*Erickson et al.*, 2000; *Ohtani et al.*, 2002a, 2002b; *Voronkov et al.*, 2004]. Analyses of several substorm observations have related the occurrence of a low-frequency instability in the near-Earth region (7–11 R_E) during the rapid growth phase of the cross-tail current sheet to the onset of current disruption [*Lui et al.*, 1992; *Ohtani et al.*, 1995; *Cheng and Lui*, 1998]. Recently, *Chen et al.* [2003] reported Wind observations of energetic ion fluxes in the near-Earth magnetotail, which bear signatures of local pressure gradient reduction.

[4] The ballooning-trigger scenario is strongly supported by linear studies of ballooning instability in the near-Earth magnetotail. These studies have been carried out at various levels of sophistication, focusing on fluid as well as kinetic effects. A mathematical theory of the linear magnetohy-

[1]Center for Plasma Theory and Computation, University of Wisconsin-Madison, Madison, Wisconsin, USA.

[2]Space Science Center and Center for Magnetic Self Organization, University of New Hampshire, Durham, New Hampshire, USA.

0148-0227/07/2006JA011991

drodynamic (MHD) ballooning mode along open flux tubes in magnetotail configuration was given by *Hameiri et al.* [1991]. The ideal MHD formulation of the ballooning mode, using both the energy principle and the eigenmode analyses, has yielded stability conditions for a variety of magnetotail configurations in the context of substorm onset [*Miura et al.*, 1989; *Lee and Wolf*, 1992; *Ohtani and Tamao*, 1993; *Pu et al.*, 1992; *Hurricane et al.*, 1995, 1996, 1997; *Bhattacharjee et al.*, 1998; *Cheng and Zaharia*, 2004; *Schindler and Birn*, 2004]. Those analyses used the approximation $k_y \rightarrow \infty$, in which limit the ballooning mode aligns with field lines and therefore is one-dimensional in nature. Linear, initial-value MHD simulations were carried out [*Wu et al.*, 1998; *Zhu et al.*, 2004] to study two-dimensional ballooning modes with finite k_y. Nonideal and kinetic effects on ballooning instability were also considered within the framework of drift and Hall MHD [*Pu et al.*, 1997; *Lee*, 1999; *Zhu et al.*, 2003] as well as gyrokinetic models [*Cheng and Lui*, 1998; *Wong et al.*, 2001; *Crabtree et al.*, 2003]. While the details of the stability picture do depend on the particular equilibrium model used for the near-Earth magnetotail as well as the nonideal effects included in the analysis, a common and robust conclusion of all these analyses is that the linear ballooning mode tends to be most unstable at near-Earth distances, consistent with the scenario of substorm onset at the near-Earth magnetotail. Furthermore, linear analyses have shown that ballooning instabilities are more favored for current sheets that are thin rather than wide [*Zhu et al.*, 2003, 2004] and at intermediate values of β ($\sim\mathcal{O}(1)$) [*Ohtani and Tamao*, 1993; *Zhu et al.*, 2003, 2004]. For higher values of β, at midtail distances and further away from Earth, the modes tend to be stabilized by strong plasma compression.

[5] Despite the observational and theoretical indication that supports the ballooning-trigger scenario, it remains to be shown that the nonlinear development of a linearly unstable ballooning mode would actually lead to the disruption of the current sheet. Two fundamental questions need to be addressed regarding the dynamics and nonlinear behavior of the mode once the configuration evolves through marginal stability. Does the nonlinear growth introduce a faster timescale than the linear phase? What is the direct consequence of the nonlinear development of the ballooning instability?

[6] Until recently, there has been no attempt to study the nonlinear evolution of the ballooning instability by rigorous analytical methods. It was assumed that this instability, which is driven by the plasma pressure gradient, is quenched at small amplitudes by the quasi-linear flattening of the pressure gradient and that its net effect will be to cause enhanced transport without a global disruption of the plasma [see, for instance, *Connor et al.*, 1984]. This assumption was contradicted by a recent theory which predicted the phenomenon of "detonation," whereby the ballooning instability grows explosively in the nonlinear regime, in the manner of a finite-time singularity, destabilizing neighboring metastable regions when the threshold for the linear ballooning instability is crossed in a small region of space [*Cowley and Artun*, 1997; *Hurricane et al.*, 1997; *Fong*, 1999]. The current disruption in a substorm onset is thought to be directly triggered by this explosive growth [*Hurricane et al.*, 1999]. The scenario of explosive nonlinear growth of ballooning modes continues to be pursued actively in the context of the substorm onset problem [*Dobias et al.*, 2004]. The explosive growth phase, however, has not been found in previous particle-in-cell simulations of the nonlinear drift-ballooning instability by *Pritchett and Coroniti* [1999] or in our recent direct MHD simulations of the Rayleigh-Taylor-Parker (RTP) instability in a line-tied low-β plasma system [*Zhu et al.*, 2006a], to which the analysis of [*Cowley and Artun*, 1997] was applied.

[7] Two preconditions must be met in any numerical test of the detonation theory. First, the system must be very close to marginal stability. Second, the system should be able to numerically resolve modes with large wave number k_y in their linear as well as nonlinear stages. We remark that simulations that are not designed to meet these conditions might make predictions that are too optimistic for macroscopic stability. Most previous simulations were not sufficiently well designed to test the predictions of the detonation theory either because of different physical focus or because of the lack of sufficient computational capability.

[8] In the study of *Zhu et al.* [2006a], direct MHD simulation results were reported for the nonlinear RTP instability of line-tied flux tubes that are close to marginal stability in the asymptotic k_y regime. In the paper of *Zhu et al.* [2006b], the limitation of the explosive nonlinear regime was specified, and a new theory for the so-called "intermediate nonlinear regime" was developed. A recent numerical solution of our new theory model and its comparison with direct MHD simulations have shown good agreement [*Zhu et al.*, 2007]. In those studies, our focus was on the line-tied RTP instability.

[9] In this paper, we report our initial results from a series of direct MHD simulations of the nonlinear development of ballooning instability in two model configurations of the near-Earth magnetotail. The simulation results reported in this paper are directly and quantitatively comparable to the detonation theory for ballooning instability in the context of substorm onset developed by *Hurricane et al.* [1997, 1999]. More importantly, these simulations have allowed us to quantify the growth and to identify the structure of the ballooning instability from the linear to the intermediate nonlinear phase in the near-Earth magnetotail. The intermediate nonlinear phase is generally defined as the phase that lies between the early nonlinear regime when the linear phase ends and the late nonlinear regime when the ideal MHD model needs to be modified to include the effects of dissipation and transport. Contrary to the predictions from previous models, the nonlinear growth of the ballooning mode, up to the intermediate phase, does not seem to introduce any faster timescale than the corresponding linear phase. On the other hand, the predictions of the detonation theory regarding the tendency to form finger-like structures in the pressure contours are well supported by our simulations. The observed nonlinear growth of the ballooning instability in these simulations may be better understood qualitatively in a newly developed theoretical framework for the nonlinear line-tied RTP instability [*Zhu et al.*, 2006b, 2007]. Instead of explosive growth, the nonlinear ballooning instability tends to produce fine-scale spatial structures, correlated with the dominant k_y mode in the linear

phase, and spatial discontinuities induced by nonlinear convection. These structures may produce their unique and observable signatures of the nonlinear ballooning instability in the magnetotail.

[10] The rest of the paper is organized as follows. In section 2, we briefly review the numerical schemes for the two MHD codes used in the simulations. We then present the simulation results for two different model configurations of the near-Earth magnetotail in sections 3 and 4, respectively. Finally, we summarize our findings and discuss remaining issues in section 5.

2. Numerical Schemes

[11] Direct MHD simulations numerically solve the full set of ideal MHD equations as a three-dimensional initial-boundary value problem. The direct simulation of ballooning instabilities of the near-Earth magnetotail has been a challenge because of the disparate spatial scales of the mode structure parallel and perpendicular to magnetic field lines. Recent developments in simulation and computing resource have made the problem tractable. We have performed the simulations using two MHD codes, NIMROD and BIC, which use different numerical schemes.

[12] NIMROD (Nonideal MHD with Rotation: Open Discussion Project) is a comprehensive three-dimensional MHD code mostly developed for the study of long-wavelength, low-frequency, nonlinear phenomena in realistic geometry [*Sovinec et al.*, 2004]. The NIMROD code numerically solves nonideal, extended MHD equations

$$\frac{\partial \mathbf{B}}{\partial t} = -\nabla \times \mathbf{E} \tag{1}$$

$$\mathbf{E} = -\mathbf{u} \times \mathbf{B} + \eta \mathbf{J} + \mathbf{H} \tag{2}$$

$$\mathbf{J} = \nabla \times \mathbf{B} \tag{3}$$

$$\frac{\partial n}{\partial t} + \nabla \cdot (n\mathbf{u}) = \nabla \cdot (D \nabla n) \tag{4}$$

$$\rho\left(\frac{\partial \mathbf{u}}{\partial t} + \mathbf{u} \cdot \nabla \mathbf{u}\right) = \mathbf{J} \times \mathbf{B} - \nabla p + \nabla \cdot \nu\rho\nabla\mathbf{u} \tag{5}$$

$$\frac{n}{\gamma - 1}\left(\frac{\partial T}{\partial t} + \mathbf{u} \cdot \nabla T\right) = -\frac{p}{2}\nabla \cdot \mathbf{u} - \nabla \cdot \mathbf{q} + Q, \tag{6}$$

where **E** is the electric field, **B** is the magnetic field, **u** is the plasma flow velocity, n is the number density, $\rho = n(m_i + m_e)$ is the mass density (m_i and m_e are the proton and electron masses, respectively), T is the temperature, $p = nT$ is the pressure, **q** is the heat flux vector, Q is the heat source density, γ is the ratio of specific heats, D is the density diffusion coefficient, v is the viscosity, η is the resistivity, and **H** is the Hall electric field. The NIMROD simulations reported in this paper, however, were carried out in the ideal MHD model by setting $\eta = 0$, $D = 0$, $Q = 0$, and $\mathbf{H} = 0$. Since the algorithm in NIMROD is not dissipative, a very small amount of viscosity v is applied to resolve the boundary layers at the foot points of line-tied flux tubes. The simulation results converge with respect to the viscosity as it approaches zero.

[13] The algorithms in NIMROD code are tailored for the stiff and anisotropic conditions found in magnetic fusion experiments. High-order finite elements are used to represent the two-dimensional poloidal plane with arbitrarily shaped boundaries. The third periodic direction is discretized using a pseudo-spectral method. In the temporal domain, the solutions are advanced with semi-implicit schemes. As a major MHD code, NIMROD has been widely employed to study nonlinear macroscopic processes in laboratory fusion plasmas. In recent years, the code has been applied to the simulation of nonlinear processes in astrophysical and space plasmas. In particular, the two-dimensional finite-element discretization in NIMROD allows the natural domain representation of various regions in magnetosphere from mesoscopic to global scales. This work is one of the first applications of NIMROD to magnetospheric physics.

[14] Another code, BIC (Ballooning-Interchange Code), has been developed to study the nonlinear MHD ballooning-interchange process in various prototypical plasma configurations [*Zhu et al.*, 2006a]. BIC solves the ideal MHD equations [as in equations (1)–(6) with nonideal terms set to zero] in a three-dimensional rectangular domain with Cartesian coordinates. The code implements an explicit fourth-order Runge-Kutta time-stepping scheme and a finite second-order spatial difference scheme. It is embedded in the PETSc (Portable Extensible Toolkit for Scientific computation) framework [*Balay et al.*, 2004], which enables us to make use of PETSc's optimized computational kernels and integrated parallelization support in tackling the stiffness of spatial scales involved in ballooning-interchange dynamics.

3. Simulations With the Voigt Model

[15] In the following discussion, we use geocentric solar magnetospheric coordinates in which x points from Earth to Sun, y points from dawn to dusk, and z points from south to north. The magnetospheric noon-midnight meridian plane lies in the x-z plane. For ballooning modes with large wave numbers in the y direction, the near-Earth region of the quiescent magnetotail can be modeled by two-dimensional magnetostatic equilibria. One such equilibrium is the model of *Voigt* [1986], which assumes that

$$p(\Psi) = \frac{k^2}{2}\Psi^2, \qquad B_{\mathrm{y}}(\Psi) = -h\Psi,$$

where Ψ is magnetic flux, p is pressure, B_{y} is the dusk-dawn component of the equilibrium magnetic field, and k and h are constant scaling factors. The Grad-Shafranov equation for the two-dimensional equilibrium then becomes linear in Ψ and can be solved analytically. For the nightside magnetosphere ($x < 0$), the solution for the equilibrium magnetic flux takes the form

$$\Psi = -\frac{M_{\mathrm{D}}}{2}\sum_{n=1}^{\infty}\cos(\eta_n z)e^{\lambda_n x}\left(1 + e^{-2\lambda_n x_{\mathrm{b}}}\right) + \Psi_{-\infty},$$

where M_{D} is the dipole moment of the Earth, $\lambda_n^2 = \eta_n^2 - k^2 - h^2$, $\eta_n = (\pi/2)(2n - 1)/z_{\mathrm{mp}}$, z_{mp} and x_{b} are tail and

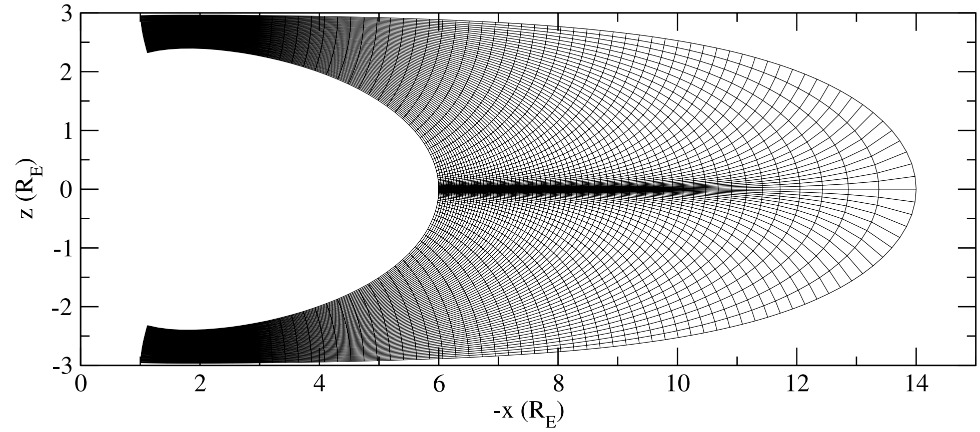

Figure 1. *x*-*z* plane of the grid generated based on Voigt model with (x_b, z_{mp}, k^2) = (6, 3, 0.15). Grid size: 64 × 128.

dayside magnetopause locations, respectively, and $\Psi_{-\infty}$ is the flux function at $x \to -\infty$ which is simply chosen to be zero. The model equilibrium is completely determined by the parameter set (x_b, z_{mp}, k^2, h). In order to focus exclusively on the unstable modes driven by the pressure gradient, we consider equilibria with zero field-aligned current, i.e., $J_{\|} = 0$. Equivalently, we set $B_y = 0$ by choosing $h = 0$. The presence of nonzero $J_{\|}$ or B_y introduces shear in the magnetic field, which tends to enhance the ballooning instability of the magnetotail [*Hurricane et al.*, 1997]. They also tend to produce coupling to kink modes, which is not included in the present treatment.

[16] We consider a particular magnetotail equilibrium by choosing $x_b = 6$, $z_{mp} = 3$ in the Voigt model, as done in previous work by *Zhu et al.* [2003, 2004]. The pressure scaling factor k^2 is used to control the overall plasma β level of the equilibrium, as well as the local β_e value, which denotes the β value at the equatorial plane and is defined as $\beta_e \equiv 2p(z = 0)/B_z^2(z = 0)$. The field lines are dipole-like at the low-β level and become more stretched and tail-like as β increases. We choose a particular configuration that is unstable to the linear ballooning instability and centered near 10 R_E in the equatorial plane, where $\beta_e = 1.208$ with $k^2 = 0.15$. The grid for the simulation is generated based on this equilibrium, so that the equilibrium magnetic field lines are aligned to one coordinate and are perpendicular to the other. For the particular grid shown in Figure 1, the domain spans the region from 6 to 14 R_E in the equatorial plane, and the flux surface that crosses the equatorial point at 14 R_E extends to the minimum x coordinate of the domain at 1 R_E from Earth. We simulate the development of the ballooning instability initiated at the center of the domain with the NIMROD code. The domain, defined by the equilibrium flux, is well represented by the two-dimensional finite-element discretization in NIMROD. We initialize the simulation with a perturbation in the x component of velocity field, localized around 10 R_E and centered on the equatorial plane. The evolution of the initial perturbation is subject to the line-tying boundary conditions at the ends of each equilibrium field line and to the no-slip wall boundary conditions on both the Earth side and the tail side of the simulation domain. Since ballooning modes are mostly localized across magnetic field lines, the boundary conditions on the flux surfaces at both sides of the domain are expected to have little effect on the modes initiated on field lines located near the center of the domain, as long as both sides of the domain are sufficiently far away from the domain center. The no-slip wall boundary conditions are therefore a choice of convenience; also, they are the first step toward more realistic boundary conditions. The value of the adiabatic index γ is chosen to be one for the evolution of the perturbation. This choice is motivated by the fact that a steady, adiabatic convection in near-Earth plasma sheet is not realistic since it will lead to the unrealistic pressure pileup (the so-called entropy catastrophe) in near-Earth magnetotail [*Erickson and Wolf*, 1980]. Observations indicate that the adiabatic index γ is a function of both time and locations in plasma sheet and ranges from 1.52 to less than 1 [*Huang et al.*, 1989; *Borovsky et al.*, 1998]. It is also found numerically convenient to choose the isothermal model for the temperature/pressure evolution by setting $\gamma = 1$. From the temperature equation in equation (6), it can be seen that the temperature/pressure evolution only involves convection when $\gamma = 1$. The choice $\gamma = 1.67$ would include the effects of compression in temperature/pressure evolution equation. Linearly, this would bring in additional stabilization due to enhanced compression, but nonlinearly, it is not expected to change the growth and structure of the ballooning modes qualitatively. Nevertheless, the effects of γ on the nonlinear ballooning instability of near-Earth plasma sheet is highly nontrivial both physically and numerically [*Zhu et al.*, 2004]. Our simulation study on the effects of the adiabatic index on nonlinear ballooning instability, with γ ranging from 0 to 1.67, is in progress and will be reported later in a separate paper. Below, we present and discuss the linear and the nonlinear phases of the ballooning mode in the simulations.

3.1. Linear Phase

[17] The Voigt equilibrium is symmetric in the y direction, and each wave number k_y is associated with a linear eigenmode. To simulate the linear phase of a ballooning instability, a single Fourier mode is excited in the y direction. The initial perturbation settles into a linearly growing mode after about 100 s. The ballooning

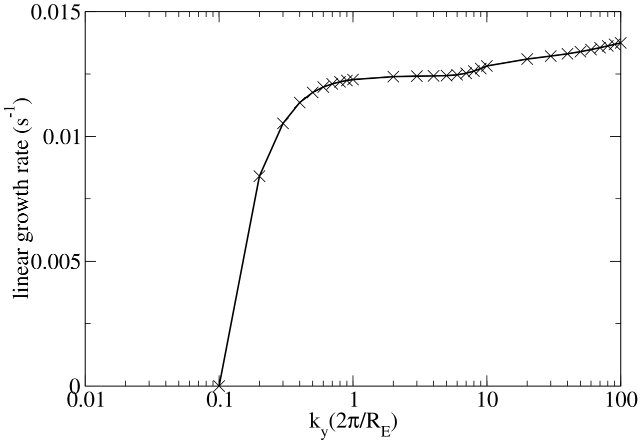

Figure 2. k_y scaling of the linear growth rate of the ballooning instability centered at $x = -10\ R_E$.

characteristics of the mode are evident in the k_y scaling of the growth rate, the mode polarization, and the perturbation pattern in x-z plane.

[18] As the k_y number becomes smaller, the linear growth rate decreases; stability is indicated at sufficiently small k_y. As k_y becomes larger, the linear growth rate increases and approaches an asymptotic value when k_y is sufficiently large (Figure 2). In reality, the presence of resistivity and finite Larmor radius (FLR) effects will produce a cutoff of the linear growth rate at the high-k_y end. The wave number $k_y^{\max}$ where the growth rate is peaked can be possibly compared with observations of precursors of a substorm onset. As shown later in section 3.2, $k_y^{\max}$ is also a signature of the nonlinear ballooning instability, which could be identified from the fully developed fluctuations prior to substorm onset.

[19] The spatial pattern of the linear ballooning instability is characterized by the scale length along, across, and perpendicular to the field line, which can be represented typically by the inverse of the corresponding wave numbers $k_\parallel^{-1}$, k_Ψ^{-1}, and $k_\perp^{-1} = k_y^{-1}$, respectively. The structure of a ballooning mode is mostly aligned along a field line and is localized in the cross and perpendicular directions, so that $k_\parallel/k_y \ll 1$, and $k_\Psi \sim \sqrt{k_\parallel k_y}$. Shown in Figure 3 are two-dimensional contours of each perturbed field in x-z plane for a linearly growing ballooning mode with $k_y = 20\pi(R_E^{-1})$. The perturbed velocity and magnetic field are also plotted as projected two-dimensional vector fields overlaid with the perturbed density and pressure contours, respectively. In addition to the spatial pattern, the contour plots of each component of the perturbed velocity and magnetic field in Figure 3 show the ballooning mode polarizations as well; that is, $u_x \sim u_z \gg u_y$ and $\tilde{B}_x \sim \tilde{B}_z \gg \tilde{B}_y$.

[20] The localization of the most unstable linear modes in the x-z plane occurs near 10 R_E in the magnetotail as shown in Figure 3. Since plasma β increases monotonically tailward from the Earth in the x direction in the near-Earth plasma sheet, the 10 R_E region maps to the intermediate plasma β regime. The localization of the most unstable linear ballooning mode in x direction is a manifestation of the localization of the most unstable linear ballooning mode in the intermediate plasma β regime [*Ohtani and Tamao*, 1993; *Zhu et al.*, 2003, 2004].

3.2. Nonlinear Phase

[21] For the nonlinear phase of the simulations, five Fourier modes in the y direction are allocated with wave numbers $k_y = 20n\pi[R_E^{-1}]$, $n = 1, \ldots, 5$. We denote the k_y spectrum of the initial perturbed u_x field as u_n, so that $u_x|_{t=0} = \Sigma_n u_n(x, z) \cos(2n\pi y/L_y)$, with $L_y = 0.1\ R_E$. We discuss three simulation cases here. The initial conditions of these cases differ only in the choice of u_n. The maximum amplitude of the u_n is set to be $10^{-3}\ u_{A0}$, where u_{A0} is the characteristic Alfvén speed of the system. While the detailed evolution depends on the initial spectrum u_n, some generic features are obtained for both temporal growth and spatial (real and spectral) patterns of the mode in the nonlinear phase.

3.2.1. Case 1: $u_n \propto \delta_{n,1}$

[22] In this case, only the $n = 1$ component of the initial perturbed u_x field is set to be nonzero. After an initial transient phase from $t = 0$ to $t = 100$, the $n = 1$ mode enters a linear growth phase, while the kinetic energies of all other $n \neq 1$ modes grow mostly through nonlinear couplings. During the linear phase of the $n = 1$ mode ($t \sim 100-200$), the kinetic energies of all the $n \neq 1$ modes remain much less than the $n = 1$ mode (Figure 4). In the nonlinear phase, the growth of all modes slows down, and all growth rates approach the same value. However, even well into the nonlinear phase, the $n = 1$ component remains dominant. This is consistent with the nonlinear mode pattern discussed below.

[23] The background fields are visibly reconfigured only when the mode evolves beyond the early nonlinear phase. As shown in Figure 4, the most prominent finger pattern develops in the contour of total pressure field in the $z = \pm 1.86\ R_E$ planes at $t = 500$ s rather than in the equatorial plane at $z = 0$. This is consistent with the structure of the linear mode for which the maximum perturbation resides on a plane between the magnetopause and the equatorial plane (Figure 3). Such a mode structure reflects the highly compressible nature of the ballooning mode discussed here. The width of the finger pattern corresponds to the half-wavelength of the corresponding linear $n = 1$ mode. In reality, the dominant n or k_y component in the ballooning mode spectrum of a linear perturbation is determined by kinetic effects, especially the FLR effect, which constrains the width of the finger pattern of the pressure field in y-z plane that may be obtained from observations. It is also worth mentioning here that the finger pattern shown in Figure 4 is actually much narrower in the y direction than it appears since the x-y aspect ratio in that plot is not drawn to scale due to a limitation of the visualization program used for those plots. The same remark applies to the two cases below as well.

3.2.2. Case 2: $u_n \propto \delta_{n,2}$

[24] The finger pattern of the pressure field in the $z = \pm 1.86\ R_E$ planes at $t = 500$ s is more pronounced in the case where only the $n = 2$ component is present in the initial perturbation of u_x field (Figure 5). The width of the finger pattern in y direction corresponds to the half-wavelength of the $n = 2$ Fourier component. At $t = 500$ s, the pressure

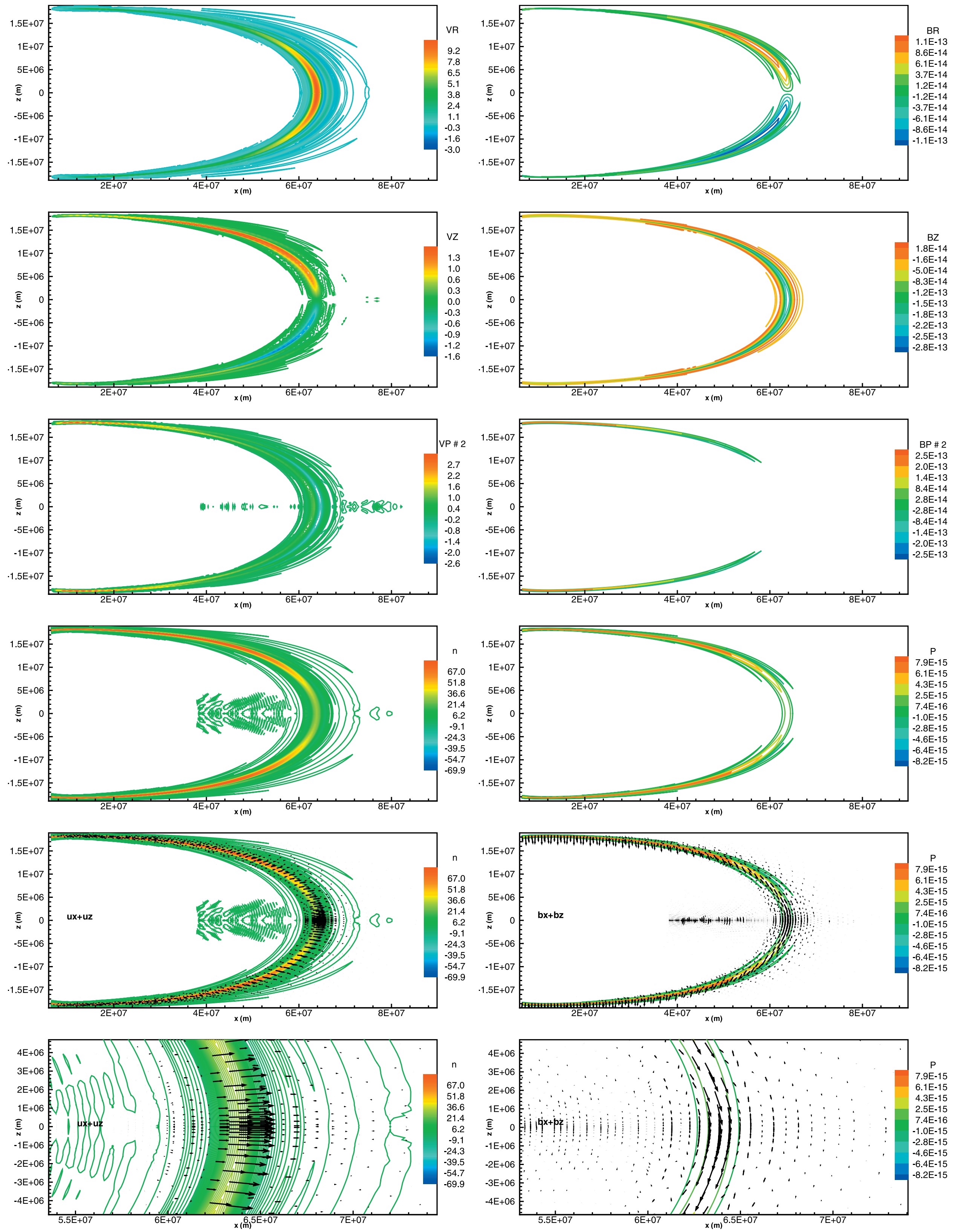

Figure 3. Two-dimensional patterns of the linear ballooning mode in *x-z* plane. Left column: Contour of u_x (row 1); u_z (row 2); u_y (row 3); $\tilde{n}$ (row 4); $\tilde{n}$ and $u_x\,\hat{x} + u_z\,\hat{z}$ vector field (row 5); zoomed view of panel in row 5 (row 6). Right column: Contour of $\tilde{B}_x$ (row 1); $\tilde{B}_z$ (row 2); $\tilde{B}_y$ (row 3); $\tilde{p}$ (row 4); $\tilde{p}$ and $\tilde{B}_x\hat{x} + \tilde{B}_z\hat{z}$ vector field (row 5); zoomed view of panel in row 5 (row 6). Note that the negative sign ($-$) in the *x*-axis label ($-$x) is dropped here (also in Figures 4–6) for convenience.

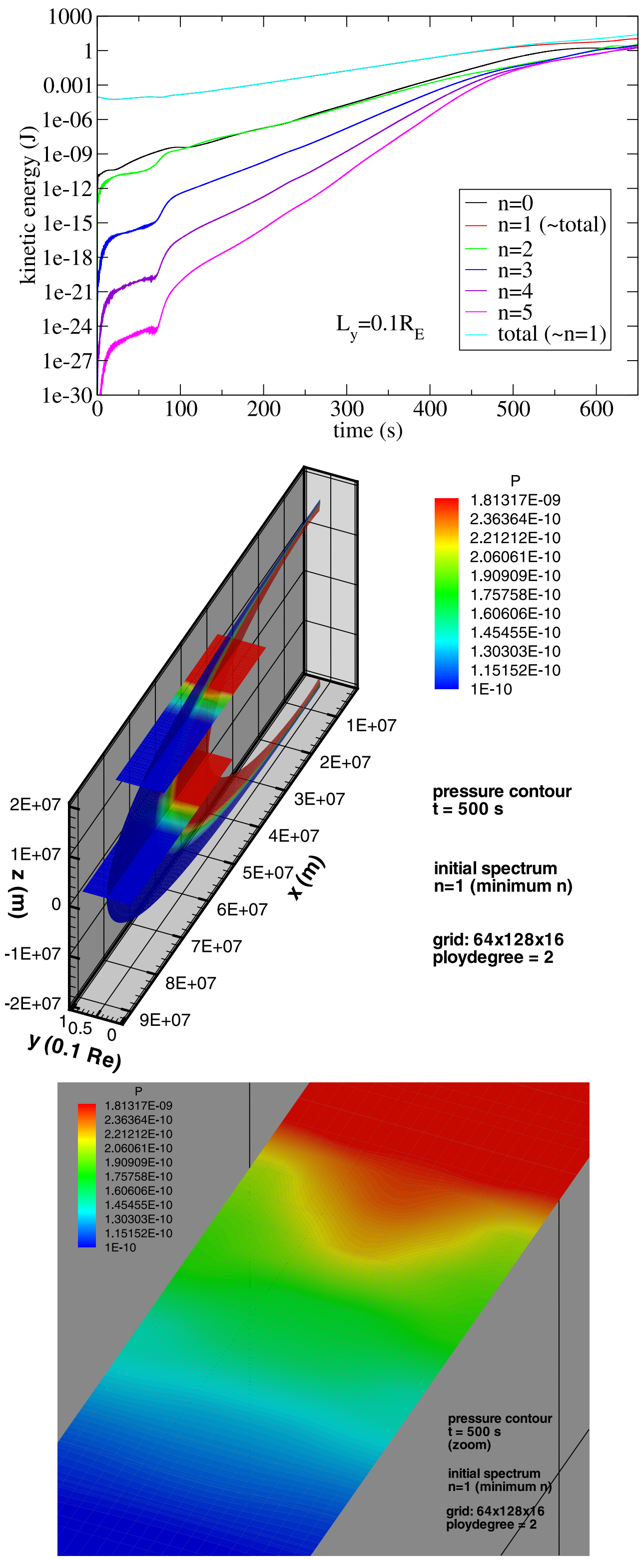

Figure 4. Case 1: Growth of kinetic energy of total perturbation and of each Fourier component in the y direction (top panel); pressure contours in $y = 0.5\ R_E$, $z = 0$, and $z = 1.86\ R_E$ planes at t = 500 s (middle panel); zoomed view of the finger formation region of the pressure contour in $z = 1.86\ R_E$ plane at t = 500 s (bottom panel).

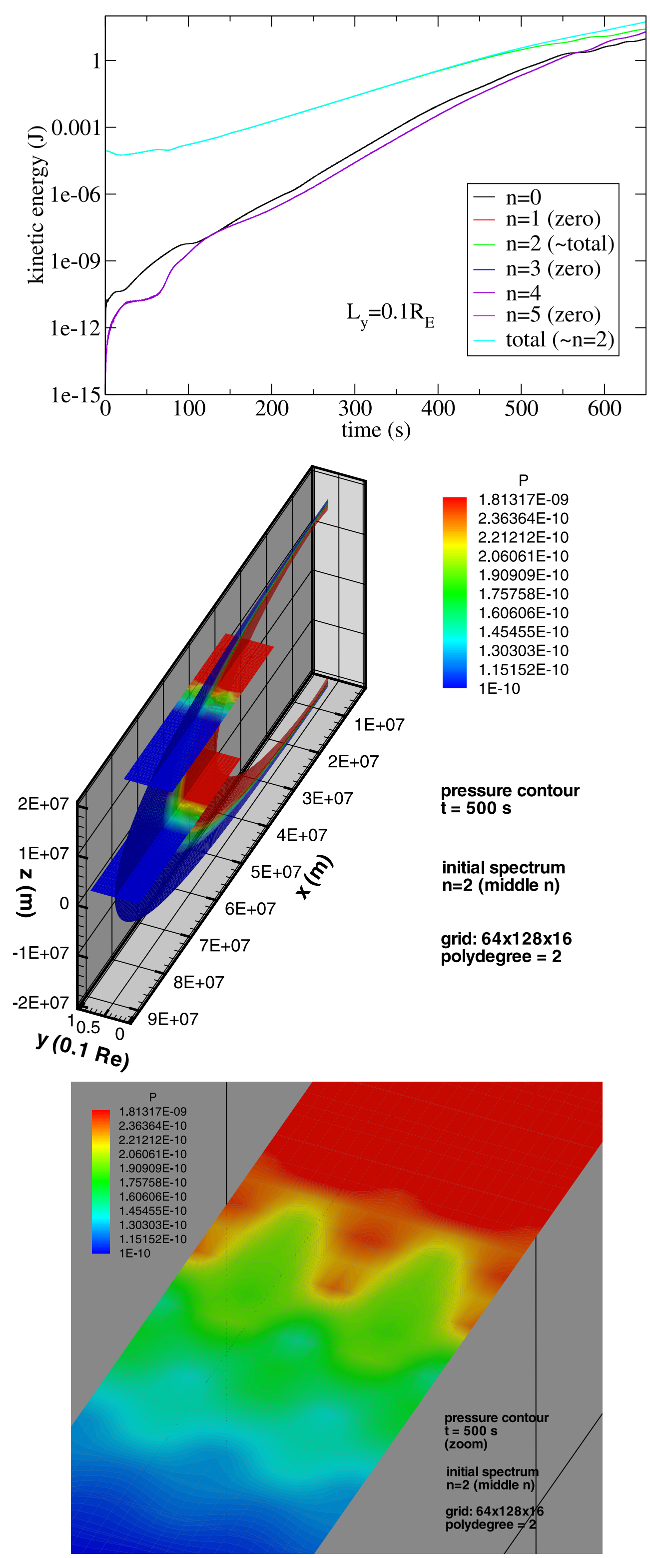

Figure 5. Case 2: Growth of kinetic energy of total perturbation and of each Fourier component in the y direction (top panel); pressure contours in $y = 0.5\ R_E$, $z = 0$, and $z = 1.86\ R_E$ planes at t = 500 s (middle panel); zoomed view of the finger formation region of the pressure contour in $z = 1.86\ R_E$ plane at t = 500 s (bottom panel).

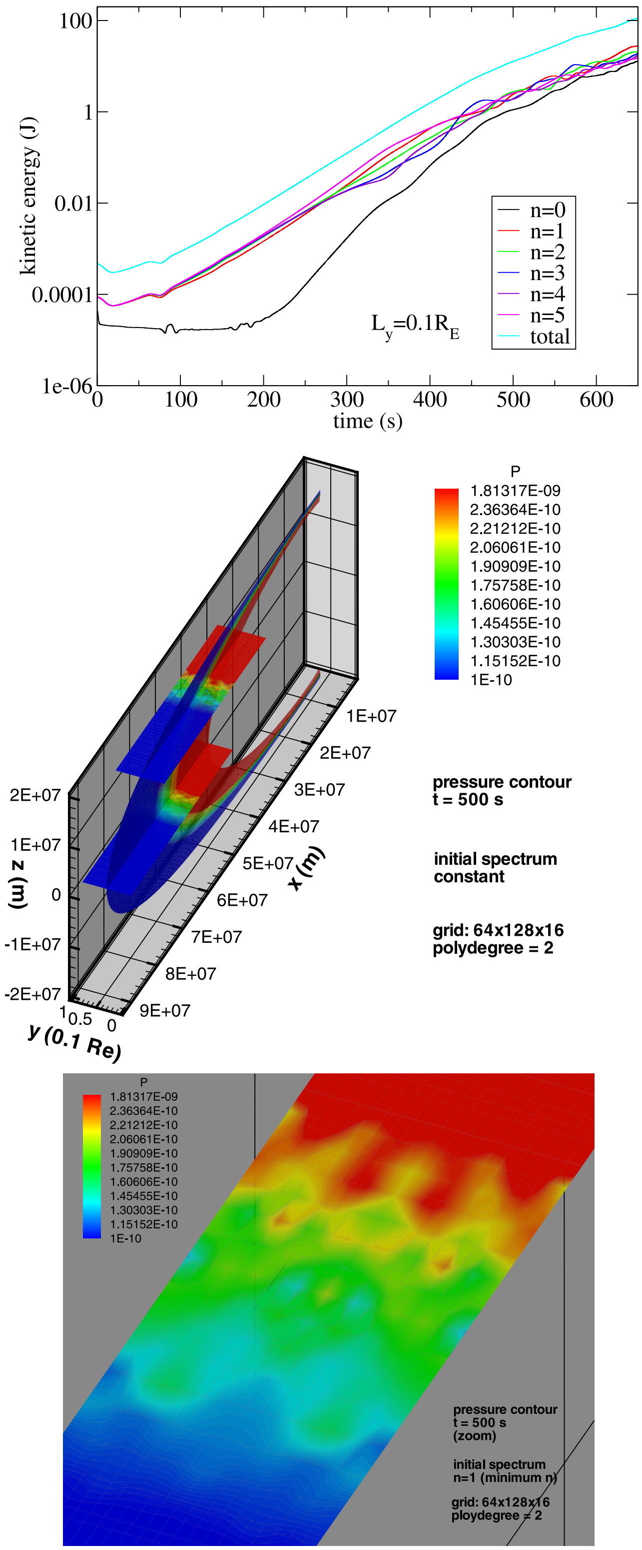

Figure 6. Case 3: Growth of kinetic energy of total perturbation and of each Fourier component in the y direction (top panel); pressure contours in $y = 0.5\ R_E$, $z = 0$, and $z = 1.86\ R_E$ planes at $t = 500$ s (middle panel); zoomed view of the finger formation region of the pressure contour in $z = 1.86\ R_E$ plane at $t = 500$ s (bottom panel).

contour in the equatorial plane ($z = 0$) remains close to that of the initial equilibrium.

[25] The distribution of energy in the different k_y components is different from the previous case when only the $n = 1$ mode is present in the initial perturbation. As shown in Figure 5, only the even-n modes are excited and grow with time, whereas the energy of all the odd-n modes remains zero throughout the linear and nonlinear phases. That behavior indicates the quadratic nature of the dominant nonlinear interaction of ballooning instability. The growth of the total energy as well as that of each (odd-) n mode slows down in the nonlinear phase, similar to the case discussed in section 3.2.1.

3.2.3. Case 3: u_n Independent of n

[26] In this case, all Fourier components of the u_x field are initiated with the same amplitude. There is a clear linear phase ($t \sim 100$–200 s) during which the k_y scaling of the linear ballooning instability is evident (Figure 6). Entering the nonlinear phase ($t > 200$ s), energy starts to flow among modes and mostly to the $n = 0$ mode. The growth of the total kinetic energy slows down. There is no one dominant Fourier component in the power spectrum in this phase. Correspondingly, during the intermediate phase ($t = 500$ s), there is no distinct mode number associated with the pressure contours in $z = \pm 1.86\ R_E$ planes (Figure 6). The finger pattern is more complex than is seen in previous two cases.

[27] One feature that is common to all three cases discussed above is that the total perturbation energy of the system continues to grow exponentially in the early nonlinear phase, followed by a slower growth in the intermediate nonlinear phase. This indicates that the timescale of a pressure gradient-driven instability in an ideal MHD model is bounded from above by its linear growth rate. The nonlinear development, up to the intermediate nonlinear phase, does not seem to introduce a faster timescale.

[28] Another common feature in the intermediate nonlinear phase is the formation in the pressure field of two-dimensional finger-like patterns in y-z off-equatorial planes. The width of the finger pattern in the y direction is proportional to the wavelength of the dominant Fourier component in that direction. The maximum length of the finger pattern in the x direction is about the size of the pressure gradient scale length $[(d\ln p/dx)^{-1}]$. As discussed earlier, the dominant wave number k_y of the linear ballooning mode spectrum can be determined by the equilibrium properties of plasma sheet during the growth phase. This prediction can be compared with observations of the precursor pulsation and the spatial structure of the ensuing nonlinear pressure fluctuation prior to substorm onset.

4. Simulations With the Box Model

[29] The nonlinear dynamics of the ballooning instability may be understood at a more fundamental level by considering the Rayleigh-Taylor-Parker (RTP) instability in the box model of the near-Earth magnetotail configuration. The box model employs a one-dimensional MHD equilibrium (a reduced two-dimensional Grad-Shafranov equilibrium) with line-tied magnetic field lines to approximate the local configuration of the near-Earth plasma sheet. A virtual gravity $-g\hat{x}$ is introduced to simulate the tension force

from the curved magnetic field of the magnetotail. The magnetic field lines in the box model are straight and support plasma pressure against gravity. The equilibrium obeys the one-dimensional force balance equation:

$$\frac{\mathrm{d}}{\mathrm{d}x}\left(p_0 + \frac{B_0^2}{2}\right) = \rho_0 \mathbf{g} \cdot \hat{x}, \quad \mathbf{g} = -g\hat{x}.$$

The field lines are tied to perfectly conducting plates placed at two boundaries of z, emulating the Earth's ionosphere.

[30] Using BIC, we integrate numerically the full set of three-dimensional, compressible ideal MHD equations directly in a rectangular domain of dimensions L_x, L_y, and L_z in the x, y, and z directions, respectively. We begin with tangential hyperbolic profiles for the initial equilibrium configuration

$$\rho_0(x) = \rho_c + \rho_h \tanh[(x + L_c)/L_\rho], \tag{8}$$

$$\mathbf{B}_0 = B_0(x)\hat{z}, \tag{9}$$

$$B_0^2(x) = B_0^2(0) + 2g\left(\rho_h L_\rho \ln\frac{\cosh(L_c/L_\rho)}{\cosh[(x+L_c)/L_\rho]} - \rho_c x\right) - 2[p_0(x) - p_0(0)] \tag{10}$$

where ρ_c is the mass density at the center of the density slope $x = -L_c$, and L_ρ is the scale length of the equilibrium density gradient. We have assumed that $p_0(x) = \rho_0(x)$; that is, the temperature is taken to be unity initially at $t = 0$. We define $p_{-\infty} \equiv p_0(x \to -\infty) = \rho_c - \rho_h$. All length scales are normalized by $L_\rho/5$, velocities by the Alfvén speed computed with the magnetic field $B_{-\infty} \equiv \sqrt{p_{-\infty}}$, time by the Alfvén timescale computed with the characteristic length scale and Alfvén speed, and pressure (and density) by $p_{-\infty}$. The computational domain is $L_x = 64$, $L_y = 0.1$, and $L_z = 128$. We choose the length L_y to be the wavelength of a linear unstable mode of large perpendicular wave number $k_y = 2\pi/L_y = 20\pi$. The initial perturbation at this fundamental wave number is chosen to be sufficiently large that it attains the intermediate nonlinear regime before the modes of higher wave number can grow to dominate the fundamental. The most unstable linear eigenmode is characterized by a displacement that is perpendicular to the equilibrium magnetic field and is even in z. For the simulation parameters chosen, the growth rate of the instability is weak and sub-Alfvénic, and its spatial structure is consistent with linear theory. The three-dimensional nonlinear simulations are performed on a Cartesian grid with a typical resolution of $256 \times 32 \times 256$ along x, y, and z, respectively. The number of grid points along y may seem relatively small, but it is worth noting that L_x:L_y:L_z = 640:1:1280, that is, $L_x \sim L_z \gg L_y$, so fewer grid points are needed along y to achieve the same quality of resolution as along x and z. We impose line-tied boundary conditions in z, no-slip, solid wall boundary conditions in x, and periodic boundary conditions in y. While there is no physical dissipation in the underlying equations, numerical diffusion is unavoidable but can be made small by running the simulations at high resolution. We have carried out simulations at various levels of resolution to test the robustness and convergence of our results.

[31] Prescribed by the parameter set $B_0(0) = 0.1$, $g = 0.1$, $L_\rho = 5$, the high-β equilibrium we choose yields an initial value of $\beta \sim 30\%$ in the pressure slope region, relevant to the near-Earth magnetotail condition. We perturb the initial equilibrium by an initial flow field $u_x|_{t=0}$, with the peak value of 0.001, in the direction of gravity and localized in the pressure slope region. The imposed perturbation splits and propagates along field lines, is reflected at the boundaries, and, after a transient phase, evolves into an exponentially growing eigenmode of the line-tied equilibrium. Figure 7 (upper panel) shows the growth of the maximum values of each velocity component. As shown, the instability continues to grow exponentially in the early and intermediate nonlinear regimes. This exponential nonlinear growth eventually slows down and shows no tendency to develop a finite-time singularity. The lower left column of Figure 7 shows the pressure profile $p(x, y = 0, z = 0)$, which is a cut of the three-dimensional pressure field along the x axis, at three typical times representing linear, early nonlinear, and intermediate nonlinear phases of the instability. The lower right column in Figure 7 shows pressure contours in the x-y plane at exactly the same time as the cut on the lower left of Figure 7 in each row, showing clear evidence of the formation of fingers protruding in the direction of (virtual) gravity. The prototypical finger, which grows exponentially in the early nonlinear regime as it penetrates into neighboring spatial regions, eventually develops a flat mushroom-type structure at its head. As the frames in the lower left column indicate, while the pressure profile (left column, top row) becomes flat (left column, middle and bottom rows) over most of the slope, the pressure gradient tends to accumulate near the lower edge of the slope (left column, bottom row), leading to the formation of a spatial discontinuity. Once formed, this coherent structure continues to propagate into neighboring regions without changing its shape much. We note that the location of the discontinuity formation is also the stagnation point of plasma flow, where all components of the velocity field reduce to zero.

[32] The RTP instability in the box model resembles the ballooning mode in the Voigt model, in both growth and structure, for initial perturbations with the same Fourier spectrum in y direction. In the above case and in case 1 in section 3.2, only the $n = 1$ Fourier component is nonzero in initial perturbation. In both cases, the perturbation grows exponentially in linear to early nonlinear phases and slows down in the intermediate nonlinear phase (Figures 4 and 7). In addition, the similarity in the formation of the finger pattern in the x-y plane is evident. However, the locations of the x-y planes where the finger patterns in pressure contours are most distinct are different in two cases. In the box model, the most prominent finger forms in the $z = 0$ plane, which is located at the middle of the line-tied field lines. These are the sites where the pressure perturbation, as well as the plasma displacement and field line bending across flux surface (or in x direction), is maximum along field lines. In the case of the Voigt model, the locations of the maximum plasma displacement and field line curvature across flux surface, which are in the $z = 0$ plane, are different from the locations of maximum pressure perturbation, which are in off-equatorial planes ($z = \pm 1.86\ R_E$, for

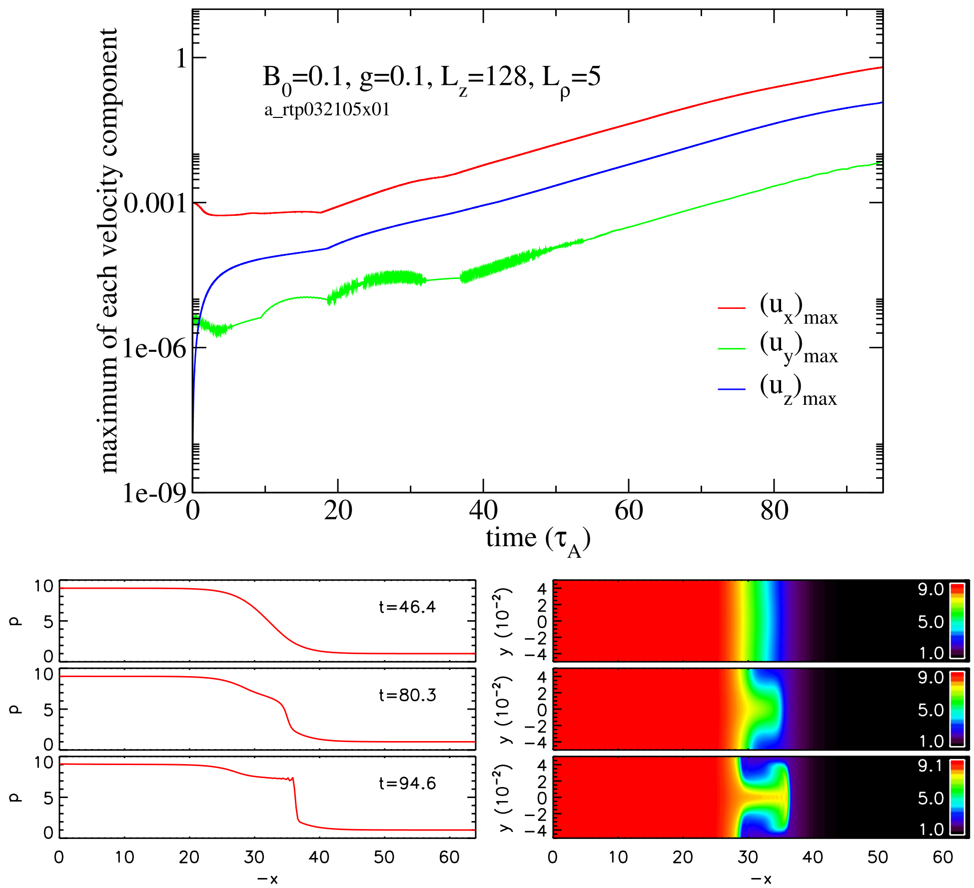

Figure 7. Case with only n = 1 Fourier component in the y direction being nonzero in initial perturbation: Growth of the maximum of each velocity component (top panel); pressure profile $p(x, y = 0, z = 0)$, which is a cut of the three-dimensional pressure field along x, at three instants of time (lower left column); pressure contours in the x-y plane (z = 0) at the same instants as in the same row (lower right column).

example). Therefore the most prominent finger patterns in pressure contour are formed not in the z = 0 plane but in the off-equatorial planes. These similarities and differences between the RTP instability in the box model and the ballooning mode in the Voigt model of the near-Earth magnetotail can also be found in other cases where the initial perturbations have different spectral content.

5. Summary and Discussion

[33] In summary, we have carried out three-dimensional direct MHD simulations for the early to intermediate nonlinear development of the ballooning instability in two model configurations of the near-Earth magnetotail. In light of recent theory development on the nonlinear RTP instability [*Zhu et al.*, 2006b, 2007], we show that finite-time singularities (also referred to as faster-than-exponential growth) are generally absent in the nonlinear phase of ballooning instability, and nonlinear growth of the instability itself does not seem to introduce faster timescales than the corresponding linear phase. The direct consequence of a growing ballooning instability, in its intermediate nonlinear phase, is the formation of fine-scale finger patterns in the y (dusk-dawn) direction and of spatial discontinuities in the x direction (or normal to a flux surface). The spatial scale of the finger pattern in the y direction, which is the width of each "finger," is related to the wavelength of the dominant Fourier component in that direction. The size of the finger pattern in the x direction (or the length of each finger) is determined by gradient scale length of the pressure or density profile in equilibrium. These characteristic nonlinear structures of the ballooning instability may be used to identify the presence of such a mode in the near-Earth magnetotail prior to the onset of a substorm.

[34] A faster timescale may come about from the coupling of the ballooning instability to other processes in the near-Earth magnetotail, such as the kink instability due to field-aligned currents, in both linear and nonlinear stages. In order to focus on the nonlinear behavior of the ballooning instability, we have deliberately considered equilibria where this coupling does not occur.

[35] The formations of the fine-scale coherent structures such as fingers and spatial discontinuities indicate the start of a regime where ideal MHD model may no longer apply and nonideal, kinetic, dissipative process and mechanisms become essential. The coupling of ballooning instability and the kinetic dissipation mechanisms within those fine structures may introduce faster timescales. In addition, the

coherent mode structure may turn turbulent with increasing nonlinearity as the instability evolves beyond intermediate phase. The enhanced turbulent transport could lead to the destruction of flux surfaces on a rapid timescale. The simulations of the late nonlinear phase of the ballooning instability are beyond the scope of the current paper and are left to future work.

[36] Another possible consequences of the nonlinear development of ballooning instability are the enhanced thinning of current sheet and the ensuing fast reconnection in the near-Earth magnetotail in the intermediate and late nonlinear phases. In our simulations, reductions in B_z around the equatorial plane have been observed in both linear and nonlinear phases, a tendency leading to further thinning of the current sheet. However, the absolute magnitude of such reduction remains relatively weak in the intermediate nonlinear phase. This suggests that the particular model configurations we choose may not be realistic enough for the study of the process of enhanced thinning of the current sheet. A more stretched current sheet configuration will be the subject of our study in the future. Furthermore, as suggested above, these simulations need to be extended to the late nonlinear regime, including other nonideal physical effects.

[37] **Acknowledgments.** This research is supported by NSF grant ATM 00-0203, NSF grant ATM-0542954, and DOE grant DE-FG02-86ER53218. Computations were performed in the National Energy Research Scientific Computing Center, which is supported by DOE under contract DE-AC03-76SF00098, and on the Zaphod Beowulf cluster which was in part funded by the Major Research Instrumentation program of the NSF under grant ATM-0420905. The authors are grateful for the discussions with J. D. Callen and S. C. Cowley.

[38] Zuyin Pu thanks Gary M. Erickson and another reviewer for their assistance in evaluating this paper.

References

Atkinson, G. (1967), The current system of geomagnetic bays, *J. Geophys. Res.*, *72*, 6063.

Balay, S., K. Buschelman, V. Eijkhout, W. D. Gropp, D. Kaushik, M. G. Knepley, L. C. McInnes, B. F. Smith, and H. Zhang (2004), PETSc users manual, *Tech. Rep. ANL-95/11-Revision 2.1.5*, Argonne National Laboratory, Argonne, Ill.

Bhattacharjee, A., Z. W. Ma, and X. Wang (1998), Ballooning instability of a thin current sheet in the high-Lundquist-number magnetotail, *Geophys. Res. Lett.*, *25*, 861–864.

Borovsky, J. E., M. F. Thomsen, R. C. Elphic, T. E. Cayton, and D. J. McComas (1998), The transport of plasma sheet material from the distant tail to geosynchronous orbit, *J. Geophys. Res.*, *103*, 20,297–20,332, doi:10.1029/97JA03144.

Chen, L.-J., A. Bhattacharjee, K. Sigsbee, G. Parks, M. Fillingim, and R. Lin (2003), Wind observations pertaining to current disruption and ballooning instability during substorms, *Geophys. Res. Lett.*, *30*(6), 1335, doi:10.1029/2002GL016317.

Cheng, C. Z., and A. T. Y. Lui (1998), Kinetic ballooning instability for substorm onset and current disruption observed by AMPTE/CCE, *Geophys. Res. Lett.*, *25*, 4091–4094.

Cheng, C. Z., and S. Zaharia (2004), MHD ballooning instability in the plasma sheet, *Geophys. Res. Lett.*, *31*, L06809, doi:10.1029/2003GL018823.

Connor, J. W., J. B. Taylor, and M. F. Turner (1984), Ideal MHD ballooning instability and scaling law for confinement, *Nucl. Fusion*, *24*, 642–647.

Cowley, S. C., and M. Artun (1997), Explosive instabilities and detonation in magnetohydrodynamics, *Phys. Rep.*, *283*, 185–211.

Crabtree, C., W. Horton, H. V. Wong, and J. W. V. Dam (2003), Bounce-averaged stability of compressional modes in geotail flux tubes, *J. Geophys. Res.*, *108*(A2), 1084, doi:10.1029/2002JA009555.

Dobias, P., I. O. Voronkov, and J. C. Samson (2004), On nonlinear plasma instabilities during the substorm expansive phase onset, *Phys. Plasmas*, *11*, 2046–2053, doi:10.1063/1.1695357.

Erickson, G. M., and R. A. Wolf (1980), Is steady convection possible in the Earth's magnetotail?, *Geophys. Res. Lett.*, *7*, 897.

Erickson, G. M., N. C. Maynard, W. J. Burke, G. R. Wilson, and M. A. Heinemann (2000), Electromagnetics of substorm onsets in the near-geosynchronous plasma sheet, *J. Geophys. Res.*, *105*, 25,265–25,290, doi:10.1029/1999JA000424.

Fong, B. H. (1999), Metastable and explosive properties of ballooning modes in laboratory and space plasmas, Ph.D. thesis. Princeton Univ., Princeton, N. J.

Frank, L. A., and J. B. Sigwarth (2000), Findings concerning the positions of substorm onsets with auroral images from the Polar spacecraft, *J. Geophys. Res.*, *105*, 12,747–12,762, doi:10.1029/1999JA000356.

Friedrich, E., J. C. Samson, I. Voronkov, and G. Rostoker (2001), Dynamics of the substorm expansive phase, *J. Geophys. Res.*, *106*, 13,145–13,164, doi:10.1029/2000JA000292.

Hameiri, E., P. Laurence, and M. Mond (1991), The ballooning instability in space plasmas, *J. Geophys. Res.*, *96*, 1513–1526.

Huang, C. Y., C. K. Goertz, L. A. Frank, and G. Rostoker (1989), Observational determination of the adiabatic index in the quiet time plasma sheet, *Geophys. Res. Lett.*, *16*, 563–566.

Hurricane, O. A., R. Pellat, and F. V. Coroniti (1995), The stability of a stochastic plasma with respect to low frequency perturbations, *Phys. Plasmas*, *2*, 289–293.

Hurricane, O. A., R. Pellat, and F. V. Coroniti (1996), Instability of the Lembége-Pellat equilibrium under ideal magnetohydrodynamics, *Phys. Plasmas*, *3*, 2472–2474.

Hurricane, O. A., B. H. Fong, and S. C. Cowley (1997), Nonlinear magnetohydrodynamic detonation: Part I, *Phys. Plasmas*, *4*, 3565.

Hurricane, O. A., B. H. Fong, S. C. Cowley, F. V. Coroniti, C. F. Kennel, and R. Pellat (1999), Substorm detonation, *J. Geophys. Res.*, *104*, 10,221.

Kisabeth, J. L., and G. Rostoker (1971), Development of the polar electrojet during polar magnetic substorms, *J. Geophys. Res.*, *76*, 6815.

Lee, D.-Y. (1999), Stability analysis of the plasma sheet using Hall magnetohydrodynamics, *J. Geophys. Res.*, *104*, 19,993–19,999.

Lee, D.-Y., and R. A. Wolf (1992), Is the earth's magnetotail balloon unstable?, *J. Geophys. Res.*, *97*, 19,251–19,257.

Lopez, R. E., and A. T. Y. Lui (1990), A multisatellite case study of the expansion of a substorm current wedge in the near Earth magnetotail, *J. Geophys. Res.*, *95*, 8009.

Lopez, R. E., H. Lühr, B. J. Anderson, P. T. Newell, and R. W. McEntire (1990), Multipoint observation of a small substorm, *J. Geophys. Res.*, *95*, 18,897.

Lui, A. T. Y. (2003), Cause of magnetospheric substorms, *Plasma Phys. Control. Fusion*, *45*, 841–852.

Lui, A. T. Y., R. E. Lopez, B. J. Anderson, K. Takahashi, L. J. Zanetti, R. W. McEntire, T. Potemra, D. M. Klumpar, E. M. Greene, and R. Strangeway (1992), Current disruptions in the near-Earth neutral sheet region, *J. Geophys. Res.*, *97*, 1461.

Miura, A., S. Ohtani, and T. Tamao (1989), Ballooning instability and structure of diamagnetic hydromagnetic waves in a model magnetosphere, *J. Geophys. Res.*, *94*, 15,231–15,242.

Ohtani, S., and T. Tamao (1993), Does the ballooning instability trigger substorms in the near-Earth magnetotail?, *J. Geophys. Res.*, *98*, 19,369.

Ohtani, S., T. Higuchi, A. T. Y. Lui, and K. Takahashi (1995), Magnetic fluctuations associated with tail current disruption: Fractal analysis, *J. Geophys. Res.*, *100*, 19,135–19,146, doi:10.1029/95JA00903.

Ohtani, S., R. Yamaguchi, H. Kawano, F. Creutzberg, J. B. Sigwarth, L. A. Frank, and T. Mukai (2002a), Does the braking of the fast plasma flow trigger a substorm?: A study of the August 14, 1996, event, *Geophys. Res. Lett.*, *29*(15), 1721, doi:10.1029/2001GL013785.

Ohtani, S., R. Yamaguchi, M. Nosé, H. Kawano, M. Engebretson, and K. Yumoto (2002b), Quiet time magnetotail dynamics and their implications for the substorm trigger, *J. Geophys. Res.*, *107*(A2), 1030, doi:10.1029/2001JA000116.

Pritchett, P. L., and F. V. Coroniti (1999), Drift ballooning mode in a kinetic model of the near-Earth plasma sheet, *J. Geophys. Res.*, *104*, 12,289–12,300.

Pu, Z. Y., R. Korth, and G. Kremser (1992), Plasma and magnetic field parameters at substorm onsets derived from GEOS 2 observations, *J. Geophys. Res.*, *97*, 19,341.

Pu, Z. Y., A. Korth, Z. X. Chen, R. H. W. Friedel, Q. G. Zong, X. M. Wang, M. H. Hong, S. Y. Fu, Z. X. Liu, and T. I. Pulkkinen (1997), MHD drift ballooning instability near the inner edge of the near-Earth plasma sheet and its application to substorm onset, *J. Geophys. Res.*, *102*, 14,397–14,406.

Roux, A., S. Perraut, P. Robert, A. Morane, A. Pedersen, A. Korth, G. Kremser, B. Aparicio, D. Rodgers, and R. Pellinen (1991), Plasma sheet instability related to the westward traveling surge, *J. Geophys. Res.*, *96*, 17,697–17,714.

Samson, J. C., L. R. Lyons, P. T. Newell, F. Creutzberg, and B. Xu (1992a), Proton aurora and substorm intensifications, *Geophys. Res. Lett.*, *19*, 2167.

Samson, J. C., D. Wallis, T. Hughes, F. Creutzberg, J. Ruohoniemi, and R. Greenwald (1992b), Substorm intensifications and field line resonances in the nightside magnetosphere, *J. Geophys. Res.*, *97*, 8495–8518.
Schindler, K., and J. Birn (2004), Mhd stability of magnetotail equilibria including a background pressure, *J. Geophys. Res.*, *109*, A10208, doi:10.1029/2004JA010537.
Sergeev, V., D. Mitchell, C. Russell, and D. Williams (1993), Structure of the tail plasma/current sheet at 11 R_E and its changes in the course of a substorm, *J. Geophys. Res.*, *98*, 17,345–17,365.
Sovinec, C., et al. (2004), Nonlinear magnetohydrodynamics simulation using high-order finite elements, *J. Comput. Phys.*, *195*, 355.
Voigt, G.-H. (1986), Magnetospheric equilibrium configurations and slow adiabatic convection, in *Solar Wind-Magnetosphere Coupling*, edited by Y. Kamide and J. A. Slavin, pp. 233–273, Terra Sci., Tokyo.
Voronkov, I. O., E. F. Donovan, P. Dobias, V. I. Prosolin, M. Jankowska, and J. C. Samson (2004), Late growth phase and breakup in the near-earth plasma sheet, in *Proceedings of the 7th International Conference on Substorms (ICS-7)*, p. 140, Levi, Finland.
Wong, H. V., W. Horton, J. W. Van Dam, and C. Crabtree (2001), Low frequency stability of geotail plasma, *Phys. Plasmas*, *8*, 2415–2424.
Wu, C. C., P. L. Pritchett, and F. V. Coroniti (1998), Hydromagnetic equilibrium and instabilities in the convectively driven near-earth plasma sheet, *J. Geophys. Res.*, *103*, 11,797.
Zhu, P., A. Bhattacharjee, and Z. W. Ma (2003), Hall magnetohydrodynamic ballooning instability in the magnetotail, *Phys. Plasmas.*, *10*, 249–258.
Zhu, P., A. Bhattacharjee, and Z. W. Ma (2004), Finte-k_y ballooning instability in the near-Earth magnetotail, *J. Geophys. Res.*, *109*, A11211, doi:10.1029/2004JA010505.
Zhu, P., A. Bhattacharjee, and K. Germaschewski (2006a), Intermediate nonlinear evolution of the Parker instability: Formation of convection-induced discontinuities and absence of finite-time singularities, *Phys. Rev. Lett.*, *96*, 065001, doi:10.1103/PhysRevLett.96.065001.
Zhu, P., C. C. Hegna, and C. R. Sovinec (2006b), Nonlinear growth of a line-tied g mode near marginal stability, *Phys. Plasmas*, *13*, 102307, doi:10.1063/1.2358505.
Zhu, P., C. C. Hegna, C. R. Sovinec, A. Bhattacharjee, and K. Germaschewski (2007), Intermediate nonlinear regime of a line-tied g mode, *Phys. Plasmas*, *14*, 055903, doi:10.1063/1.2671230.

A. Bhattacharjee and K. Germaschewski, Space Science Center and Center for Magnetic Self Organization, University of New Hampshire, 39 College Road, Durham, NH 03824, USA. (amitava.bhattacharjee@unh.edu; kai.germaschewski@unh.edu)

C. C. Hegna, C. R. Sovinec, and P. Zhu, Center for Plasma Theory and Computation, University of Wisconsin-Madison, 1500 Engineering Drive, Madison, WI 53706, USA. (hegna@cae.wisc.edu; sovinec@engr.wisc.edu; pzhu@wisc.edu)